IPEM
Institute of Physics and
Engineering in Medicine

PAPER • OPEN ACCESS

Ex vivo validation of non-invasive phase correction for transspine focused ultrasound: model performance and target feasibility

View the [article online](#) for updates and enhancements.

You may also like

Physics in Medicine & Biology

OPEN ACCESS

Ex vivo validation of non-invasive phase correction for transspine focused ultrasound: model performance and target feasibility

David Martin[1,2,*] ⓘ, Rui Xu[1,2] ⓘ, Max Dressler[1] ⓘ and Meaghan A O'Reilly[1,2]

[1] Sunnybrook Research Institute, Sunnybrook Health Sciences Centre, 2075 Bayview Avenue, Toronto, ON M4N 3M5, Canada
[2] Department of Medical Biophysics, Temerty Faculty of Medicine, University of Toronto, 101 College Street Suite 15-701, Toronto, ON M5G 1L7, Canada
[*] Author to whom any correspondence should be addressed.

E-mail: david.martin@sri.utoronto.ca and moreilly@sri.utoronto.ca

Keywords: focused ultrasound, ray acoustics, spine

Supplementary material for this article is available online

Abstract

Objective. To evaluate the feasibility of transspine focused ultrasound using simulation-based phase corrections from a CT-derived ray acoustics model. *Approach.* Bilateral transspine focusing was performed in *ex vivo* human vertebrae with a spine-specific ultrasound array. Ray acoustics-derived phase correction was compared to geometric focusing and a hydrophone-corrected gold standard. Planar hydrophone scans were recorded in the spinal canal and three metrics were calculated: target pressure, coronal and sagittal focal shift, and coronal and sagittal Sørensen–Dice similarity to the free-field. *Post hoc* analysis was performed *in silico* to assess the impact of windows between vertebrae on focal shift. *Main results.* Hydrophone correction reduced mean sagittal plane shift from 1.74 ± 0.82 mm to 1.40 ± 0.82 mm and mean coronal plane shift from 1.07 ± 0.63 mm to 0.54 ± 0.49 mm. Ray acoustics correction reduced mean sagittal plane and coronal plane shift to 1.63 ± 0.83 mm and 0.83 ± 0.60 mm, respectively. Hydrophone correction increased mean sagittal similarity from 0.48 ± 0.22 to 0.68 ± 0.19 and mean coronal similarity from 0.48 ± 0.23 to 0.70 ± 0.19. Ray acoustics correction increased mean sagittal and coronal similarity to 0.53 ± 0.25 and 0.55 ± 0.26, respectively. Target pressure was relatively unchanged across beamforming methods. *In silico* analysis found that, for some targets, unoccluded paths may have increased focal shift. *Significance.* Gold standard phase correction significantly reduced coronal shift and significantly increased sagittal and coronal Sørensen–Dice similarity ($p < 0.05$). Ray acoustics-derived phase correction reduced sagittal and coronal shift and increased sagittal and coronal similarity but did not achieve statistical significance. Across beamforming methods, mean focal shift was comparable to MRI resolution, suggesting that transspine focusing is possible with minimal correction in favourable targets. Future work will explore the mitigation of acoustic windows with anti-focus control points.

1. Introduction

Focused ultrasound (FUS) is a promising tool for targeted, non-invasive treatment of cancer and other diseases. Applications include the use of FUS-induced microbubble excitation for selective, reversible disruption of the blood–brain barrier, the layer of tightly-junctioned endothelial cells that prevents many therapeutic agents from diffusing from the bloodstream into the brain (Hynynen *et al* 2001). While FUS modulation of the blood–brain barrier is now being explored clinically (Carpentier *et al* 2016, Lipsman *et al* 2018, Chen *et al* 2020, Beccaria *et al* 2021, Meng *et al* 2021, Huang *et al* 2022, Rezai *et al* 2024), the application of FUS to diseases of the spinal cord, and the functionally equivalent blood-spinal cord barrier (BSCB), has received less attention and is limited by a lack of methods for focusing through the vertebral arch. It has been shown, however, that FUS can modulate the BSCB in animal models (Shimamura *et al* 2005,

Wachsmuth *et al* 2009, Ando *et al* 2011, Oakden *et al* 2015, Weber-Adrian *et al* 2015, Payne *et al* 2017, Song *et al* 2017, O'Reilly *et al* 2018, Montero *et al* 2019, 2024, Fletcher *et al* 2019, Fletcher *et al* 2020, Cross *et al* 2021, Bhimreddy *et al* 2023) and facilitate spinal cord neuromodulation (Liao *et al* 2021a, 2021b, 2022 Kim *et al* 2022, Tsehay *et al* 2023, Wang *et al* 2023, Song *et al* 2024). Despite promising pre-clinical work, there remain significant challenges to overcome in order to achieve precise FUS delivery through the intact human spine. To date, published attempts at BSCB opening in a large animal model have been limited to a single study, in which two geometrically focused transducers were used to induce BSCB permeability *in vivo* in Yorkshire pigs (Fletcher *et al* 2020). BSCB opening was confirmed by Evans Blue dye extravasation, but opening success varied with target position, and some cases exhibited substantial focal deflection. The potential for focal deflection was later confirmed in benchtop experiments using an *ex vivo* porcine spine, where mean focal shift was 2.7 mm.

Wave-front aberrations occur when ultrasound propagates through heterogenous media, particularly when the variations in sound speed are high, as is the case with bone (Fry 1977, Fry and Barger 1978). While soft tissue at body temperature has a longitudinal speed of sound comparable to water ($\sim$1500 m s^{-1}), cancellous and cortical bone can have speeds of sound exceeding 2000 m s^{-1} and 3500 m s^{-1}, respectively (Hasgall *et al* 2022). This can have therapeutic consequences, as an aberrated focus may miss its intended target or fail to deliver sufficient energy for its intended application. In transskull applications, steerable ultrasound arrays composed of individually driven elements have been combined with CT-based numerical models to correct for bone-induced phase shifts and attenuation (Clement and Hynynen 2002a, Aubry *et al* 2003). Others have proposed the use of custom 3D printed acoustic lenses to correct the beam distortions (Maimbourg *et al* 2018, Jiménez-Gambín *et al* 2019, 2020).

Although similar in many respects to transskull FUS, transspine focusing is complicated by various anatomical factors. These include the irregular shape of the spine compared to the relatively smooth skull, the narrow width of the spinal canal, and the presence of acoustic windows between vertebrae. Further, due to the incident angles of sound on the vertebral arch, there may be non-negligible shear wave transmission. In this regard, the transspine focusing problem has parallels to transcostal FUS, where the rib cage causes focal aberrations and, in the case of long transmission pulses, undesirable bone heating due to variable absorption (Aubry *et al* 2008).

In recent years, simulation methods have been developed to facilitate transspine aberration correction. In 2018, Xu and O'Reilly presented a steady-state ray acoustics model for transvertebral ultrasound propagation, incorporating acoustic properties previously derived from human skull samples (Pichardo *et al* 2011, Xu and O'Reilly 2018). Ray acoustics is an attractive simulation method for transspinal applications because it accounts for refraction, mode conversion, and reflection at interfaces, all of which are non-negligible in spine, while incurring a lower computational cost than full-wave, elastic time-domain models. Unlike a time-domain model, however, the ray acoustics model used here assumes steady-state conditions. Despite this limitation, Xu *et al* reported a relatively low mean error (1/16th of a wavelength) when using ray acoustics to calculate vertebra-induced time shifts with a short sonication pulse (Xu *et al* 2021). However, this preliminary implementation of ray acoustics-derived transvertebral beamforming was limited to unilateral focusing and considered single vertebrae rather than stacked columns. As such, the feasibility and limitations of phase-corrected FUS in the spine have yet to be experimentally explored. Here, we present an evaluation of bilateral transspine beamforming methods using a spine-specific array prototype. We experimentally demonstrate the feasibility of array-based focusing through segments of an *ex vivo* human vertebral column and evaluate the performance of the multi-layered ray acoustics model for calculating phase corrections.

2. Materials and methods

2.1. Device specifications and manufacturing

A custom 128-element phased array was built for the experiments (figure 1). This prototype device constitutes the transvertebral components of a previously-described, 256-element, spine-specific design (Xu and O'Reilly 2020) and was fabricated following procedures described in Xu *et al* (2021). The array was assembled in-house using annular lead zirconate titanate transducers (7.5 mm outer diameter, 5.3 mm inner diameter, 4.5 mm height, purchased from Del Piezo Specialties, LLC, West Palm Beach, FL, USA) integrated into a 3D-printed plastic housing. The transducers were radially poled with electrodes on the inner and outer surfaces, and were driven in lateral (length) mode. Array elements were cylindrically focused around the vertical axis and tilted superiorly/inferiorly to provide geometric focusing in the elevation direction (figure 1). Elements were positioned to capitalize on optimal sound transmission pathways (Xu and O'Reilly 2020). A tinned copper lead ground wire was silver epoxied (GPC-251LV, Creative Materials; Ayer, MA, USA) to the inner surface of each element and a corresponding signal wire was epoxied to the outer surface. These
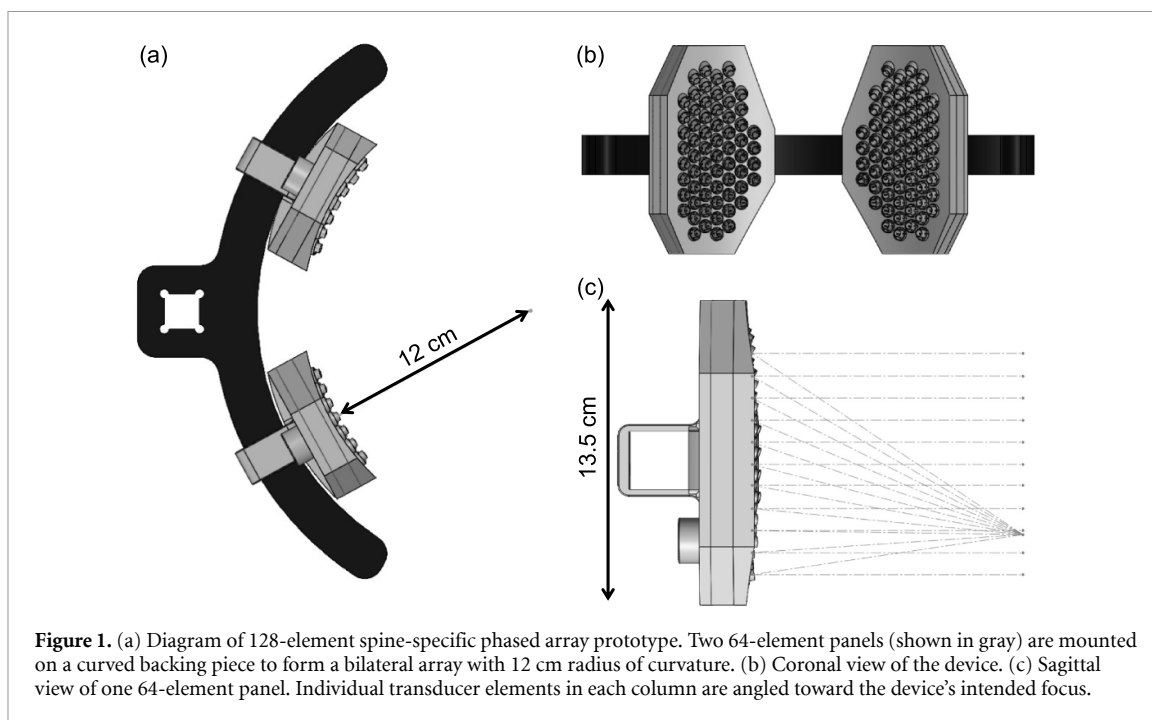
Figure 1. (a) Diagram of 128-element spine-specific phased array prototype. Two 64-element panels (shown in gray) are mounted on a curved backing piece to form a bilateral array with 12 cm radius of curvature. (b) Coronal view of the device. (c) Sagittal view of one 64-element panel. Individual transducer elements in each column are angled toward the device's intended focus.

connections were then reinforced and waterproofed with marine epoxy (LePage; Henkel Corporation, Dusseldorf, Germany).
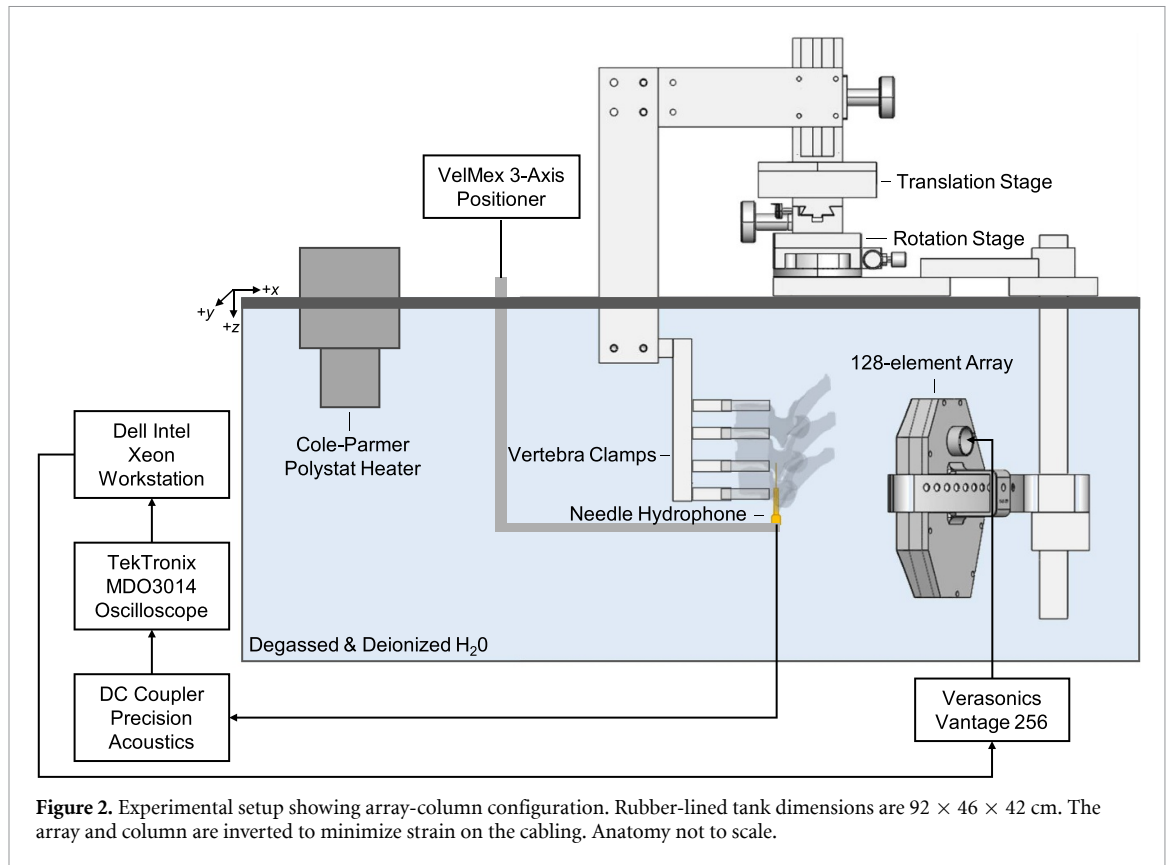
Elements were backed with a PZT/epoxy mixture (DL-57 Del Piezo Specialties/ 301 Epoxy; EPO-TEK, Billerica, MA, USA; 3:1 ratio) to improve bandwidth. The array was parylene coated with a ∼15 μm layer. Signal and ground wires for each element were soldered to micro-coaxial cables which terminated at an ITT Cannon DL5-260RW6B connector (ITT Cannon; Irvine, CA, USA). A custom circuit board was used for matching circuits, and element-specific inductor-capacitor circuits were soldered for each channel to match each element at 400 kHz to 50 Ω impedance and 0° phase (circuit components purchased from DigiKey; Thief River Falls, MN, USA). The circuit board was then connected to a Verasonics Vantage 256 low frequency research ultrasound system (Verasonics; Kirkland, WA, USA) with a second ITT Cannon. Post-construction testing determined that 116 of 128 elements were functional (∼90%). Although it is possible for the presence of dead elements to impact the distribution of the acoustic field, measurements of the free-field show symmetry in the lateral (coronal) plane (figure 4).

2.2. Experimental setup

Benchtop experiments were conducted in a rubber-lined tank (dimensions 92 × 46 × 42 cm) filled with degassed deionized water maintained at 37 °C with a Polystat immersion circulator (Cole-Parmer; Québec City, QC, Canada). The assembled array was mounted inside the tank on a custom rigid plastic frame as shown in figure 2. All experiments were performed with prior approval of the Sunnybrook Research Ethics Board (Project ID: 2693).

Thoracic vertebrae from a specimen of rehydrated, formalin-fixed, *ex vivo* adult human spine were used in the benchtop focusing experiments (Osta International; White Rock, BC, Canada). The sex, medical history, and age of the donor at time of death were unknown, but CT-based measurements of the vertebral body volumes were between the average male and average female (Limthongkul *et al* 2010, Xu and O'Reilly 2018). There were no obvious signs of pathology or degeneration. This specimen had previously been reconstituted by submersion in 10% buffered formalin for several months in order to restore the acoustic properties of the spine to close to its *in vivo* values (Fry and Barger 1978, White *et al* 2007). Following reconstitution, vertebrae underwent degassing in a vacuum chamber in degassed, deionized water over several weeks (Xu and O'Reilly 2018).

Each experiment used a column of three adjacent vertebrae (T1-T3, T4-T6, T7-T9, or T10-T12). Customized holders were 3D printed for each column, permitting consecutive vertebrae to be stacked with vertebra-specific disk separations and fixed in place in a neutral orientation (Busscher *et al* 2010). Holders were designed by stacking the vertebral meshes in Matlab (MathWorks; Natick, MA, USA), converting the stacked meshes to a binary mask, and taking its inverse. The inverse mask was manually cropped until 4 distinct plates remained: one moulded to the superior vertebral body of the first vertebra in the column, one

Figure 2. Experimental setup showing array-column configuration. Rubber-lined tank dimensions are $92 \times 46 \times 42$ cm. The array and column are inverted to minimize strain on the cabling. Anatomy not to scale.

moulded to the inferior vertebral body of the last vertebra in the column, and two moulded to the spaces between vertebral bodies of adjacent vertebrae. The masks of the plates were converted to stereolithography files and 3D printed.

At the start of each experiment day, vertebrae were arranged in a stacked column and degassed for 2 hours in deionized, degassed water in a vacuum chamber (Nalgene vacuum chamber, Fisher Scientific; Gast, Benton Harbor, MI, USA). A 3-axis positioning stage and 360-degree rotation stage (Edmund Optics; Barrington, NJ, USA) were mounted on top of an acrylic frame, and the stacked column was affixed to an arm descending from the positioning stages into the tank. This allowed the column of vertebrae to be translated and rotated within the tank space. The positioning stages were manually adjusted until the geometric focus of the array was approximately centred within the canal, and all stages were locked except for the vertical translation stage. Each of the 4 columns of vertebrae was sonicated at 8 positions (2 mm vertical spacing) for a total of 32 unique array-column configurations (figure 3). Efforts were made to place targets within regions of the canal that were fully occluded by the vertebral laminae. In practice, this resulted in the most superior target in each segment being located near the vertical midpoint of the column, with some variation across segments due to differences in freedom of movement within the canal.

Transducers were driven with a 5-cycle Gaussian windowed pulse generated with the Verasonics software's arbitrary pulse generator function. A short pulse was chosen to mitigate standing waves in the spinal canal (Fletcher and O'Reilly 2018). The origin of the experimental setup was defined at the geometric focus of the phased array and was kept fixed regardless of vertebral column position. The experimental coordinate system was defined according to the conventions of the stepping motor system, with the x-axis corresponding to the sagittal direction and the yz-plane corresponding to the coronal anatomical plane.

A 0.5 mm diameter needle hydrophone (Precision Acoustics; Dorchester, England), oscilloscope (Tektronix MDO3014; Beaverton, OR, USA) and electronic three-axis positioning system (VelMex; Bloomfield, NY, USA) were used to record the pressure field around the origin at a 10 MHz sampling rate. Raster scans of the pressure field were recorded in the sagittal (xz) and coronal (yz) planes (6×6, 0.25 mm step size, centered on origin). These dimensions represent the maximum range that the hydrophone could be consistently maneuvered across all 4 columns without colliding with the canal wall. The axes of the raster scans are defined according to the convention of the stepping motor system. As such, in contour plots of the raster scans, the $+z$ direction is anatomically superior to the origin (towards the head), the $+x$ direction is anatomically posterior to the origin (towards the back), and the $+y$ direction is anatomically to the right side of the body.
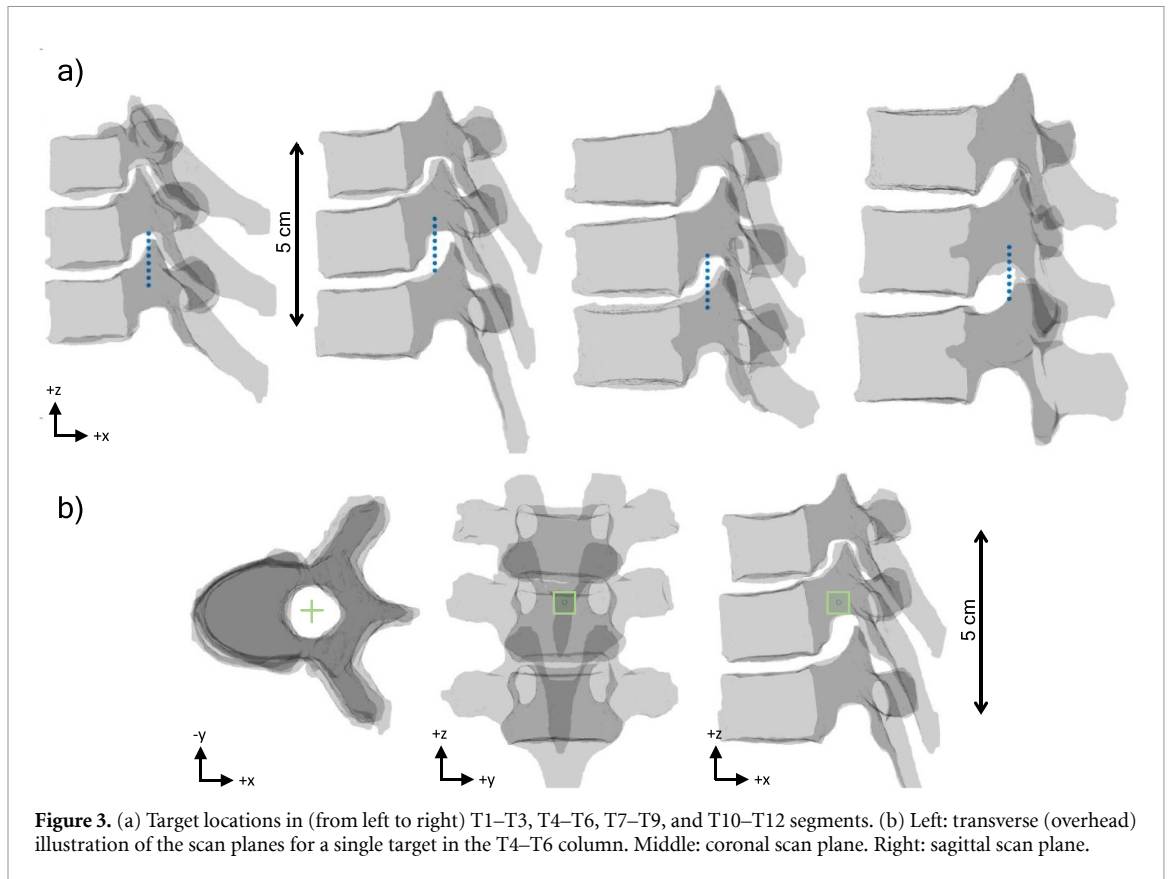
Figure 3. (a) Target locations in (from left to right) T1–T3, T4–T6, T7–T9, and T10–T12 segments. (b) Left: transverse (overhead) illustration of the scan planes for a single target in the T4–T6 column. Middle: coronal scan plane. Right: sagittal scan plane.

2.3. Hydrophone-corrected focusing

Geometric focusing was achieved by driving array elements sequentially at 70 V and recording the resulting pressure signal at the origin. Cross-correlation was used to identify the driving pulse within each recorded waveform and thus determine time-of-arrival. Arrival times were used to apply time delays to each element such that the peaks would align at the array's geometric focus when driven in unison. Experimentally-derived focusing delays were chosen over analytically-calculated delays based on element position relative to the geometric focus, as an analytical calculation would be unable to account for errors in element positions in the manufactured array or variation in impulse response and frequency content across individual elements.
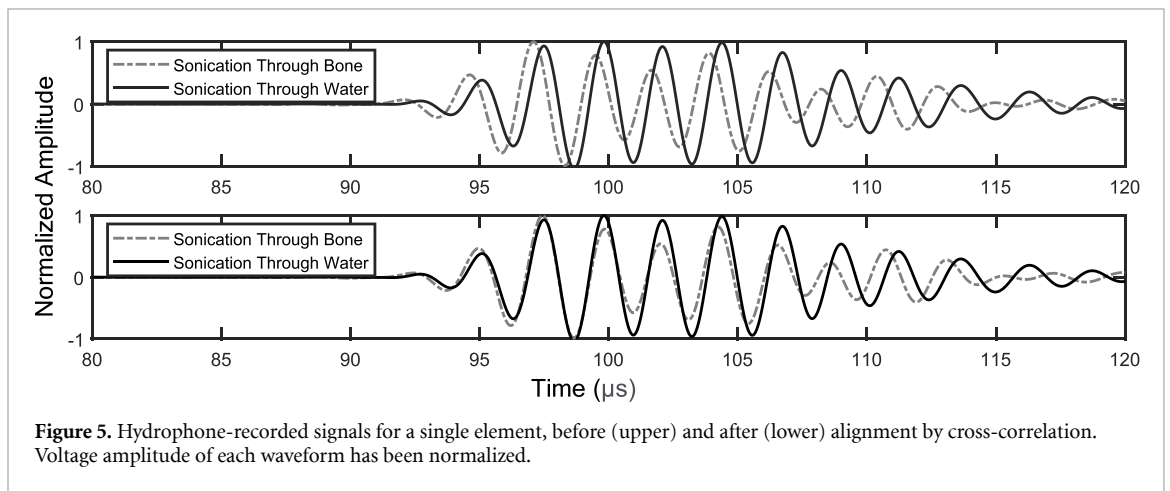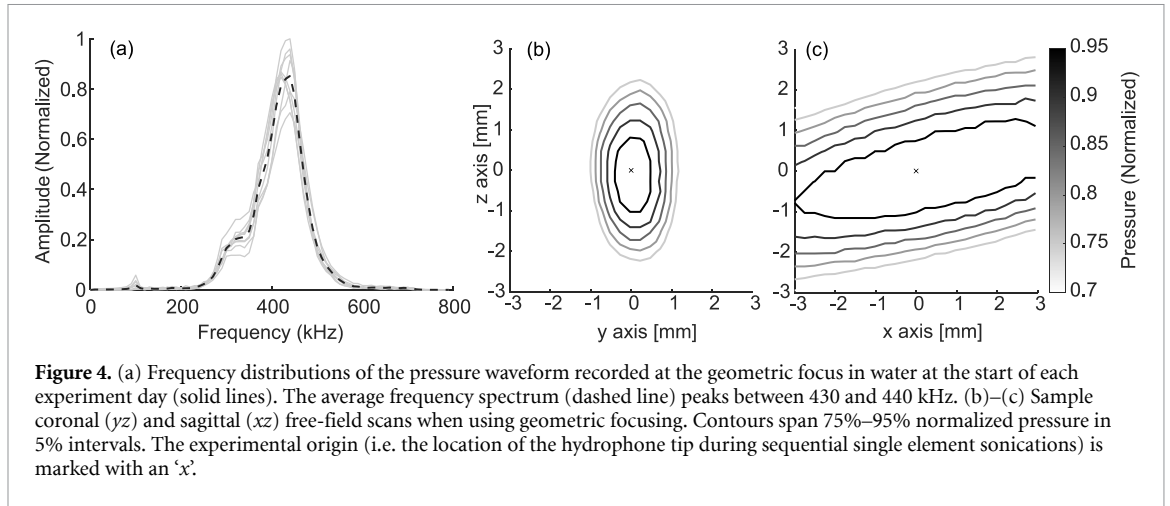
Driving amplitudes were modulated element-wise to account for variability in impulse response and ensure that individual elements made similar contributions to the total received pressure at the origin. For a given functional element, input voltage was multiplied by an apodization factor between 0 and 1, calculated as,

$$A_{eq} = \frac{A_{min}}{A_0} \tag{1}$$

where A_0 is the peak positive voltage recorded at the origin during a given functional element's sonication in water and A_{min} is the lowest peak positive voltage recorded at the origin across all functional elements.

The geometric focusing delays and amplitude equalization factors were applied to the array, and the elements were driven in unison to produce a pressure focus. Sagittal and coronal scans of the pressure field in water were recorded at the start of each experimental day as a baseline (figure 4), along with the pressure waveform at the geometric focus. Fourier analysis was performed on raw waveforms to obtain frequency spectra, and the average frequency distribution was found to be between 430 and 440 kHz, slightly higher than the array's intended driving frequency of 400 kHz (figure 4). This frequency shift may be attributed to variation in impulse response across transducer elements. Assuming an average lamina thickness of 5.4 mm and bulk sound speed of 1670 m s^{-1} in vertebral bone (Xu and O'Reilly 2022), the estimated phase error resulting from the frequency shift is approximately 1%, or 1/100th of a wavelength.

For each vertebral column-array configuration, the vertebral column was positioned in the tank after free-field scans. Sagittal and coronal scans of the pressure field were recorded to provide a baseline measurement of the distortion produced by the vertebral column. Hydrophone-corrected focusing was achieved with a second set of sequential sonications, this time with the vertebral column present. For each

Figure 4. (a) Frequency distributions of the pressure waveform recorded at the geometric focus in water at the start of each experiment day (solid lines). The average frequency spectrum (dashed line) peaks between 430 and 440 kHz. (b)–(c) Sample coronal (*yz*) and sagittal (*xz*) free-field scans when using geometric focusing. Contours span 75%–95% normalized pressure in 5% intervals. The experimental origin (i.e. the location of the hydrophone tip during sequential single element sonications) is marked with an '*x*'.

Figure 5. Hydrophone-recorded signals for a single element, before (upper) and after (lower) alignment by cross-correlation. Voltage amplitude of each waveform has been normalized.

element, the bone case signal was cross-correlated with the free-field signal to find the time delay that aligned the two waveforms (figure 5). In each case, the cross-correlation window was limited to the location of the water case time-of-arrival plus or minus one cycle. The extracted spine-induced time delay was then added to the geometric time delay for each element to correct for the presence of aberrating bone when focusing to the canal.

2.4. Numerical model: inverse simulations for benchtop aberration correction

All simulations were performed in Matlab. The phased array was registered to the simulation space using a blunted needle affixed to the arm of the stepping motor. Eight positions were recorded on the surface of the array's housing unit and registered to corresponding locations on a 3D mesh of the array in simulation space using the Horn transform (Horn *et al* 1988).

Individual vertebrae were imaged with a CT scanner (Aquilone One, Toshiba; Tokyo, Japan) at 0.5 mm isotropic resolution. Vertebrae were segmented in ITK-SNAP and three-dimensional meshes were generated from binary masks of the CT images at $\lambda/10$ discretization, λ being the wavelength of sound in water at 400 kHz (Yushkevich *et al* 2016). Longitudinal sound speed maps were generated voxel-wise (also at $\lambda/10$ discretization) using a density-dependent relationship previously established for vertebral laminae (Xu and O'Reilly 2022):

$$c_L(\rho) = 0.35(\rho - \rho_w) + c_{L,w} \, \text{m s}^{-1} \tag{2}$$

where c_L is longitudinal sound speed, ρ is the density of a given voxel, ρ_w is the density of water, and $c_{L,w}$ is the longitudinal speed of sound in water at 37 °C. Shear speed of sound was set to a constant fraction of the longitudinal speed such that $c_s = 1400/2550 \, c_L$ (Shahar *et al* 2007). Attenuation coefficients for each voxel were generated by interpolating previously established frequency- and density-dependent values for human skull to 400 kHz (Pichardo *et al* 2011, 2017).

Vertebrae meshes were stacked in simulation to replicate the configuration of a stacked column in the benchtop setup. Once a column was positioned in the tank, the needle hydrophone tip was used to record the relative position of four points on the base of the anatomically superior clamp in the stack. The Horn transform (Horn *et al* 1988), was then used to register these points to corresponding locations on a 3D mesh of the clamped column in simulation space, allowing the benchtop orientation of the array and vertebral column to be replicated *in silico*. The use of 3D-printed, column-specific clamps ensured that the relative positions of the vertebrae in a given column was preserved between the benchtop configuration and the simulation space.

Simulation corrected focusing was performed with a steady-state, multilayered ray acoustics model (Xu and O'Reilly 2018). The model does not consider reflections within the vertebral canal. Element delays were generated using an 'inverse' simulation, in which sound is propagated from the target location (in this case, the experimental origin) through the spine to the array surface. The simulation medium was populated with masks of density, longitudinal and shear speeds of sound, and longitudinal and shear acoustic attenuation coefficients. The inverse simulation was performed with and without vertebrae in place to obtain the spine-induced phase shift for each element. Simulations were performed in a parallel implementation on an NVIDIA GeForce GTX 1060 graphics card (NVIDIA; Santa Clara, CA, USA), housed in a Dell Precision T7810 desktop computer (Dell Technologies; Round Rock, TX, USA) equipped with an Intel Xeon E5-2620 CPU (Intel; Santa Clara, CA, USA). Total computation time for a single, registered therapeutic target was ~15 min. Simulation on the GPU accounted for approximately 85% of the computation time (5–6 s per element), while the remaining 15% was spent on initialization of the simulation space.

To minimize the impact of protruding structures such as the spinous and transverse processes on the model output, distinct inverse simulations were run for each transducer element in the array. In each case, a ray was traced between the element centre and the point source at the origin. A cylindrical radius of 7.5 mm was defined around the ray, and only mesh points contained within the cylinder were included in the simulation. This radius is equal to the diameter of a single array element and encapsulates the relevant section of the lamina considered in each inverse simulation. A point source with zero phase and unit magnitude was placed at the target, and sound (400 kHz) was propagated through the vertebral bone to a discretized mesh of the element surface. While previous implementations of the ray acoustics model have considered only a single layer of bone, in this study a second layer of bone was added on propagation paths where the ray tracing radius intersected multiple vertebrae.

Phase delays for each element were calculated by subtracting the conjugated phase of the water case result from the conjugated phase of the vertebra case result. Phase differences were converted to time delays that were applied to the array experimentally to correct for bone-induced focal distortion.

2.5. Simulation-corrected focusing and field measurements

Simulation-corrected transspine focusing was performed with ray acoustics-derived corrections. In both cases, time delays were applied to each element and voltage amplitude was apodized with amplitude equalization factors derived from the free-field measurements. Coronal and sagittal raster scans of the pressure field were recorded with the needle hydrophone and stepping motors. The amplitude at each grid point in the raster scan was recorded as the peak positive voltage of the averaged waveform on the oscilloscope (8 sample averaging). A total of 32 targets were evaluated in the four separate three-vertebra columns.

2.6. Raster scan analysis

The targeting accuracy of each focusing method was quantified by the shift in the weighted centroid of the 90% contour in each plane (r_{90}) relative to the free-field measurement. For example, in the sagittal (xz) plane, the weighted contour shift is reported in x (x_{90}) and z (z_{90}) as well as in the xz-plane ($r_{90} = \sqrt{x_{90}^2 + z_{90}^2}$). x_{90} and z_{90} are defined by equation (3),

$$(x_{90}, z_{90}) = \left(\frac{\sum (I(x_i, z_i) x_i)}{\sum I(x_i, z_i)}, \frac{\sum (I(x_i, z_i) z_i)}{\sum I(x_i, z_i)} \right) \tag{3}$$

where $I(x_i, z_i) \geqslant 0.9$ to restrict weighting to values greater than the 90% of the maximum pressure. The 90% contour was chosen due to the limited scan range achievable in the canal, where the 50% and 70% contours were often partially cut off by the restricted field of view. Similar benchtop studies of *ex vivo* skull specimens have used a comparable metric, defining targeting error has been defined as the distance between the voxel of highest pressure and the target location (Leung *et al* 2021, 2022, Manuel *et al* 2024).

Focal pressure was evaluated as peak positive pressure at the target location, p_{target}. Reported values were normalized to the peak free-field pressure.

The Sørensen–Dice similarity coefficient of the 90% contour was used as an additional metric of targeting accuracy and focal quality. This metric measures overlap between two binary images A and B and is therefore sensitive to changes in the shape, size, and position of the focus relative to the water case. The Sørensen–Dice coefficient is defined as:

$$\text{Dice coefficient} = 2 * \frac{|A \cap B|}{(|A| + |B|)}. \tag{4}$$

The Dice coefficient ranges from 0 to 1, with 0 indicating no overlap between the images and 1 indicating perfect overlap (Dice 1945, Sørensen 1948). In this study, images A and B are the binary masks of the 90% contour in the water case planar scan and a given corrected case planar scan, respectively. A perfectly targeted, perfectly shaped restoration of the 90% contour would therefore have a Sørensen–Dice coefficient of 1.

Finally, normalized cross-correlation was used as an overall metric of field similarity. Normalized cross-correlation measures the similarity of two signals at different offsets from one another, returning a correlation coefficient between -1 and 1. The normalized cross-correlation matrix $\gamma(u, v)$ for an image f and a template t is given by:

$$\gamma(u, v) = \frac{\sum_{x,y} \left[f(x, y) - \bar{f}_{u,v} \right] \left[t(x - u, y - v) - \bar{t} \right]}{\sqrt{\left\{ \sum_{x,y} \left[f(x, y) - \bar{f}_{u,v} \right]^2 \sum_{x,y} \left[t(x - u, y - v) - \bar{t} \right]^2 \right\}}} \tag{5}$$

where $\bar{f}_{u,v}$ is the mean of $f(x, y)$ in the region under the template. In the case of two-dimensional images of equal size, the value of interest is found at the centre of the matrix of normalized cross-correlation coefficients (Lewis 1995). In this study, normalized cross-correlation was used to compare planar field scans from each focusing trial to the water case field. A perfect restoration of the free-field focus would therefore have a normalized cross-correlation of 1.

2.7. Statistical analysis

In benchtop focusing experiments, statistical analysis was performed to compare results from the various correction methods to the geometric focusing baseline. One-way analysis of variance (ANOVA) was performed to determine whether there were differences in mean targeting error, mean target pressure, mean Sørensen–Dice coefficient, or mean normalized cross correlation among the three groups. If a difference was detected, ANOVA was followed by *post hoc* testing to look for differences in the means of each pair of groups. Results of the ANOVA and *post hoc* tests are shown in section 3.2.

2.8. Post hoc analysis of target favorability and model performance

Additional analysis was conducted *post hoc* to identify 'least favourable' targets, where all correction methods failed to improve targeting, 'most favourable' targets, where deflection away from the intended target was minimal, and 'underperforming' targets, where simulation-corrected beamforming noticeably underperformed relative to the gold standard. The sagittal plane Sørensen–Dice coefficient of the 90% contour was chosen as the metric for this analysis, since the sagittal plane consistently showed larger targeting errors than the coronal plane.

Least favourable targets included trials where the sagittal Sørensen–Dice coefficient returned a value of zero (i.e. zero overlap with the ideal 90% contour) for all beamforming methods, while most favourable targets were limited to trials where the sagittal Sørensen–Dice coefficient returned a value greater than 0.7 for all beamforming methods. Underperforming targets were classified as trials where hydrophone-corrected focusing increased the sagittal Sørensen–Dice coefficient by more than 25% relative to the geometric baseline, while ray acoustics phase correction either decreased the sagittal Sørensen–Dice coefficient, had no impact on the sagittal Sørensen–Dice coefficient, or increased the sagittal Sørensen–Dice coefficient by less than 10%. Although these criteria were chosen arbitrarily, the categorization nevertheless provides some insight into the position-dependent nature of transspine focal distortion and phase correction performance.

2.9. Post hoc analysis of unoccluded paths

During benchtop experiments, it was observed that, for some targets, the field in the canal was impacted by unoccluded propagation paths through the paralaminar spaces. Forward pressure field simulations were performed with the ray acoustics model to identify cases where unoccluded propagation was a possible confounding factor/focal aberrator. To avoid committing the inverse crime, forward simulations were performed at a lower mesh discretization ($\lambda/8$) than the inverse simulations used for phase correction ($\lambda/10$).

Forward simulations were performed using ray acoustics-derived phase corrections without amplitude modulation. Three-dimensional focal shift in the 90% contour was calculated as $r_{90} = \sqrt{x_{90}^2 + y_{90}^2 + z_{90}^2}$), where x_{90}, y_{90}, and z_{90} are defined as:

$$(x_{90}, y_{90}, z_{90}) = \left(\frac{\sum(I(x_i, y_i, z_i)\, x_i)}{\sum I(x_i, y_i, z_i)}, \frac{\sum(I(x_i, y_i, z_i)\, y_i)}{\sum I(x_i, y_i, z_i)}, \frac{\sum(I(x_i, y_i, z_i)\, z_i)}{\sum I(x_i, y_i, z_i)} \right). \tag{6}$$

Transspine and direct contributions to the field were simulated separately, making it possible to estimate the fraction of focal shift attributed to unoccluded paths as:

$$\text{direct contribution} = \frac{r_{90_{\text{direct}}}}{r_{90_{\text{direct}}} + r_{90_{\text{transvertebral}}}}. \tag{7}$$

As a means of validating field prediction performance, forward simulations were run using free-field geometric delays. Sagittal and coronal slices were extracted from the simulations at the target location and compared to the experimental raster scans with the two-dimensional zero-lag normalized cross-correlation and the Sørensen–Dice coefficient of the 70% and 90% contours. Simulated sagittal and coronal shifts in the weighted centroid of the 70% and 90% contour were also calculated and compared to the experimental measurements.

3. Results

3.1. Benchtop results: focal distortion in sagittal and coronal planes

Each beamforming method was tested in 32 targets vertically spanning the thoracic spine. Sagittal and coronal scans of the pressure field from each focusing attempt were analysed in Matlab. Peak positive pressure was normalized to an unoccluded (i.e. no vertebra present) free-field scan performed at the start of each experiment, and contours were plotted from 75% to 95% in 5% intervals. Sample plots of transspine sagittal field scans from three trials are shown in figure 5.

Sagittal and coronal shift r_{90}, Sørensen–Dice similarity, normalized cross-correlation, and normalized target pressure were calculated for each field profile. Tables 1–3 display mean and standard deviation for each metric, while table 4 reports outputs of the statistical analysis.

Across all beamforming methods, the average shift in the centroid of the sagittal 90% contour was approximately double the average shift in the centroid of the coronal 90% contour. This difference between planes may be driven by a relatively large mean shift in the anterior-posterior (x) direction in the sagittal plane, which even in the hydrophone-corrected case was greater than 1 mm (table 1). In the coronal plane, the shift in the centroid of the 90% contour was most prominent in the superior-inferior (z) direction, while mean shift in the left-right (y) direction was below 0.25 mm for all correction types (table 2).

Large standard deviations were observed in sagittal and coronal shift across all beamforming methods, with sagittal shifts greater than 3 mm recorded even in some hydrophone-corrected cases. This underscores the strong position-dependence of the beam distortions, with some targets subject to much greater deflection than others. Figure 6 displays sample contour plots of a minimally, moderately, and severely distorted focus.

Hydrophone correction produced the highest average Sørensen–Dice coefficient and normalized cross-correlation in both planes. Standard deviations for these metrics were high as well, with some targets reporting a Dice coefficient of zero (i.e. no overlap in the 90% contour between the transspine measurement and the free-field measurement) for all beamforming methods.

Average target pressure p_{target} showed little variation across beamforming methods, hovering at approximately 40% of the peak free-field pressure (table 3).

3.2. Statistical analysis and significance testing

One-wave ANOVA was performed to determine whether there was a significant difference ($p < 0.05$) in the means among the corrections methods tested for each metric. In cases where the ANOVA returned $p < 0.05$, *post hoc* testing was performed to test for differences in the means of each pair of correction methods. Complete ANOVA results are shown in table 4.

Following ANOVA, *post hoc* tests were performed for all metrics except sagittal 90% contour shift and target pressure. The hydrophone-corrected gold standard produced significant ($p < 0.05$) differences in coronal 90% contour shift (r_{90}), sagittal and coronal normalized cross-correlation, and sagittal and coronal dice similarity coefficient of the 90% contour. Ray acoustics beamforming produced no significant changes relative to the geometric baseline. *Post hoc* test results are summarized in table 5.

Table 1. Sagittal (*xz*) plane focal shift, Sørensen–Dice similarity, and normalized cross-correlation in benchtop focusing experiments. Shifts are reported in the 90% contour (x_{90}, z_{90}, r_{90}). All values reported as mean ± standard deviation.

	x_{90} (mm)	z_{90} (mm)	r_{90} (mm)	*Dice coeff.*	*NCC*
Geometric	-0.61 ± 1.35	-0.45 ± 1.18	1.74 ± 0.82	0.45 ± 0.22	0.57 ± 0.31
Hydrophone	-0.61 ± 1.25	-0.19 ± 0.85	1.40 ± 0.82	0.60 ± 0.22	0.76 ± 0.23
Ray acoustics	-0.81 ± 1.28	-0.13 ± 1.05	1.63 ± 0.83	0.53 ± 0.25	0.65 ± 0.32

Table 2. Coronal (*yz*) plane focal shift, Sørensen–Dice similarity, and normalized cross-correlation in benchtop focusing experiments. Shifts are reported in the 90% contour (y_{90}, z_{90}, r_{90}). All values reported as mean ± standard deviation.

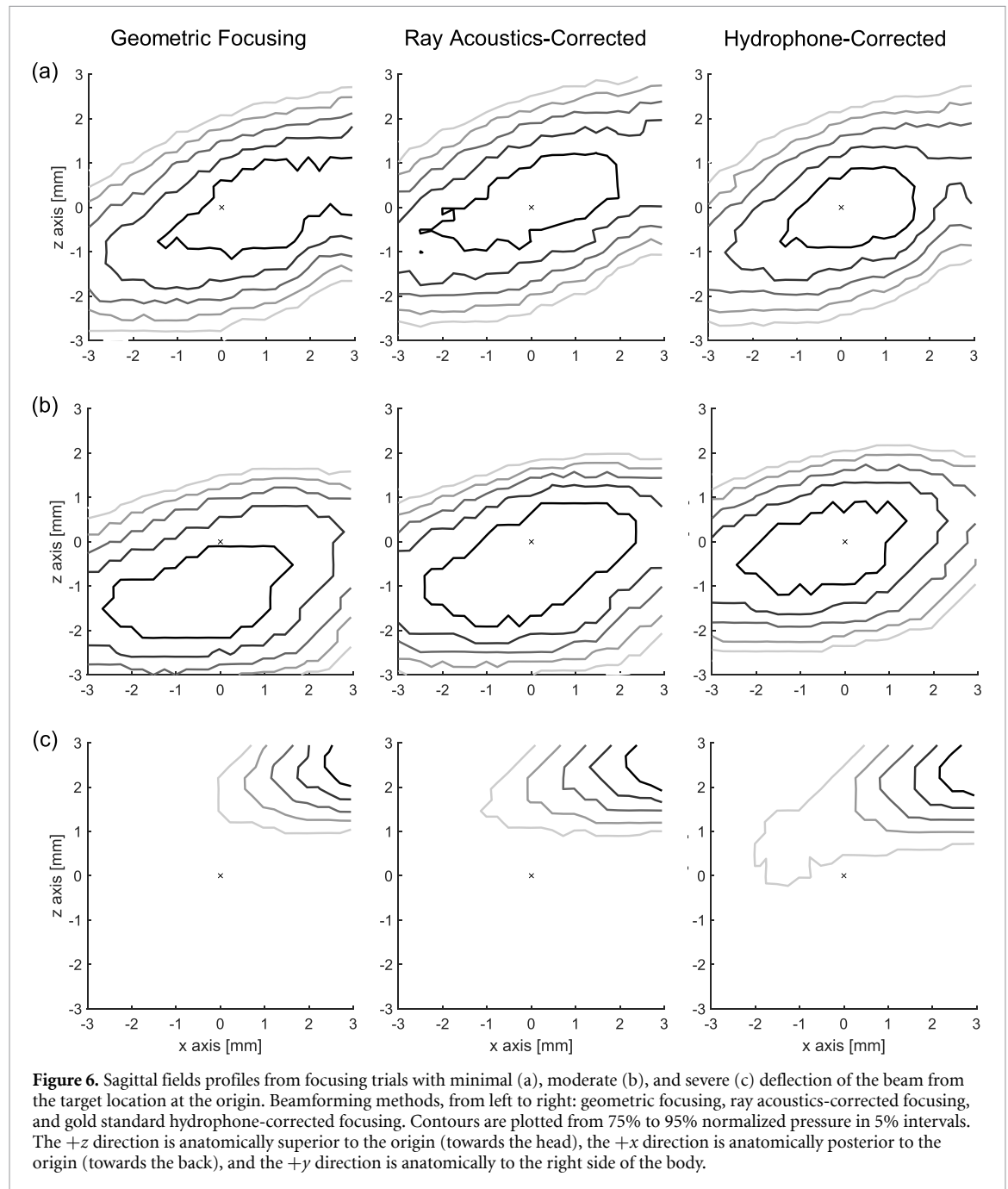|	y_{90} (mm)	z_{90} (mm)	r_{90} (mm)	*Dice coeff.*	*NCC*
Geometric	-0.02 ± 0.16	-0.22 ± 1.22	1.07 ± 0.63	0.48 ± 0.22	0.87 ± 0.06
Hydrophone	0.00 ± 0.12	-0.03 ± 0.72	0.54 ± 0.49	0.68 ± 0.19	0.93 ± 0.04
Ray acoustics	-0.10 ± 0.20	0.02 ± 1.01	0.83 ± 0.60	0.55 ± 0.26	0.88 ± 0.08

Figure 6. Sagittal fields profiles from focusing trials with minimal (a), moderate (b), and severe (c) deflection of the beam from the target location at the origin. Beamforming methods, from left to right: geometric focusing, ray acoustics-corrected focusing, and gold standard hydrophone-corrected focusing. Contours are plotted from 75% to 95% normalized pressure in 5% intervals. The +*z* direction is anatomically superior to the origin (towards the head), the +*x* direction is anatomically posterior to the origin (towards the back), and the +*y* direction is anatomically to the right side of the body.

Table 3. Target pressure p_{target}. All values reported as mean $\pm$ standard deviation. All values have been normalized to the peak free-field pressure.
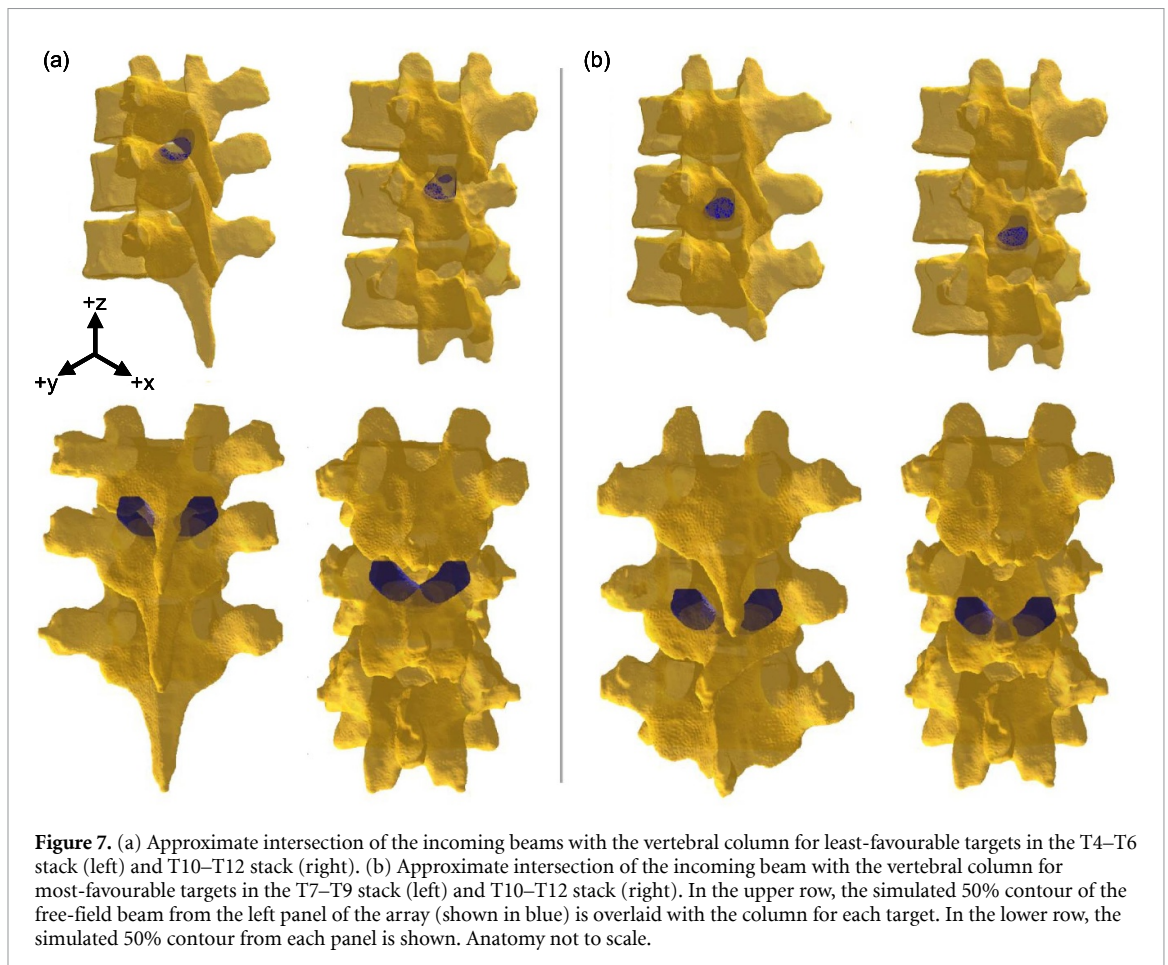
	p_{target}
Geometric	0.39 ± 0.10
Hydrophone	0.41 ± 0.11
Ray acoustics	0.38 ± 0.09

Table 4. ANOVA results for all focusing metrics. Significant ANOVA results ($p < 0.05$) are shown in bold.

	F-Statistic	*p-value*
Sagittal r_{90}	1.38	0.26
Coronal r_{90}	6.62	**<0.01**
Sagittal dice	3.44	**0.03**
Coronal dice	6.29	**<0.01**
Sagittal NCC	3.44	**0.04**
Coronal NCC	6.67	**<0.01**
p_{target}	0.88	0.42

Table 5. Results of post hoc tests. Significant results ($p < 0.05$) are shown in bold.

	p-value (Geo.—Hyd.)	*p-value (Geo.—R. Acoustics.)*	*p-value (Hyd.—R. Acoustics)*
Coronal r_{90}	**<0.01**	0.23	0.12
Sagittal dice	**0.03**	0.33	0.46
Coronal dice	**<0.01**	0.49	0.06
Sagittal NCC	**0.03**	0.52	0.29
Coronal NCC	**<0.01**	0.97	**<0.01**

Figure 7. (a) Approximate intersection of the incoming beams with the vertebral column for least-favourable targets in the T4–T6 stack (left) and T10–T12 stack (right). (b) Approximate intersection of the incoming beam with the vertebral column for most-favourable targets in the T7–T9 stack (left) and T10–T12 stack (right). In the upper row, the simulated 50% contour of the free-field beam from the left panel of the array (shown in blue) is overlaid with the column for each target. In the lower row, the simulated 50% contour from each panel is shown. Anatomy not to scale.

Figure 8. Histogram of three-dimensional focal shift attributed to unoccluded paths in forward pressure simulations with ray acoustics phase correction.

3.3. Post hoc analysis of target favorability and model performance

Out of 32 trials, two targets had a sagittal Sørensen–Dice coefficient of zero (i.e. no overlap with the 90% contour of the ideal water case field) across all beamforming methods. Figure 7(a) depicts the approximate orientation of the incoming beam relative to the vertebral column in each case. For both targets, it is hypothesized that the aberrations are caused by paralaminar gaps between consecutive vertebrae. These acoustic windows allow unattenuated and potentially guided sound waves to enter the canal, creating an off-target lobe that can be of equal or greater amplitude than the transspine contributions at the intended target. The impact of an off-target acoustic window is visible in figure 6(c), which displays the sagittal profiles for the unfavourable T4–T6 target depicted in figure 7(a).

In three focusing trials, the sagittal Sørensen–Dice coefficient was greater than 0.7 across all beamforming methods, suggesting that minimal correction was required to achieve a coherent transspine focus. All three targets were found in the lower thoracic vertebrae (two in the T10–T12 column and one in T7–T9), which have taller laminae and shorter spinous processes than upper thoracic vertebrae. The sagittal contour plots for one of these favourable targets, in the T10–T12 column, have already been shown in figure 6(a). Figure 7(b) depicts the approximate orientation of the incoming beam relative to the vertebral column for two of the three most-favourable targets. The remaining target was immediately adjacent to the displayed T10–T12 target and has therefore been omitted from the figure.

The sagittal Sørensen–Dice coefficient was also used to identify three cases where simulation-corrected focusing substantially underperformed relative to the gold standard. These were targets where hydrophone-corrected focusing increased the sagittal Sørensen–Dice coefficient by more than 25% relative to the geometric baseline, while ray acoustics phase correction either decreased the sagittal Sørensen–Dice coefficient, had no impact on the sagittal Sørensen–Dice coefficient, or increased the sagittal Sørensen–Dice coefficient by less than 10%. In two of the three cases where ray acoustics-corrected focusing underperformed relative to the gold standard, the beam appears to intersect an acoustic window on its path to the canal. In the remaining case, the beam intersects the steeply angled spinous process rather than the relatively flat laminae.

3.4. Post hoc direct contribution simulations

Forward focusing simulations of the ray-acoustics corrected case were performed to explore the impact of direct contributions through the paralaminar acoustic windows. Figure 8 displays a histogram of the estimated 90% contour shift attributed to direct contributions across all 32 targets. In the majority of cases, the impact of unoccluded paths was negligible, while in the most extreme cases, unoccluded direct contributions increased focal shift by several millimetres. In cases where the direct contributions moved the focus closer to the intended target, the shift attributed to the direct contribution is negative.

Finally, sagittal and coronal profiles of the simulated pressure fields were compared to real experimental results to validate the accuracy of the forward simulation. Although the steady-state ray acoustics model is not intended to simulate short pulses, it predicted the centroid of the 70% contour within a millimetre in both planes and had coronal and sagittal Dice similarity scores of 0.81 and 0.79, respectively, when compared to experimental results at the 70% contour level. Performance decreased at the 90% contour level, with sagittal centroid error increasing to greater than 1 mm and Dice similarity dropping below 0.60 in both planes (table 6).

Table 6. Validation of forward pressure simulation accuracy. Distance between simulation-predicted and experimentally measured weighted centroid of the 70% contour (r_{70}) and 90% contour (r_{90}) in the sagittal and coronal planes. Sørensen–Dice similarity coefficient between the simulation-predicted and experimentally measured 70% and 90% contours in the sagittal and coronal planes.

	$error_{r_{70}}$ (mm)	$error_{r_{90}}$ (mm)	*Dice* 70	*Dice* 90
Sagittal	0.81 ± 0.49	1.25 ± 0.91	0.81 ± 0.12	0.52 ± 0.20
Coronal	0.65 ± 0.30	0.80 ± 0.37	0.79 ± 0.07	0.57 ± 0.16

4. Discussion

4.1. Sagittal and coronal shift of various focusing methods

Of the two tested beamforming methods, only the hydrophone-corrected gold standard produced a statistically significant difference compared to the geometric focusing baseline. Hydrophone-corrected focusing significantly reduced average 90% contour shift (r_{90}) in the coronal plane, as well as significantly increasing both sagittal and coronal Sørensen–Dice coefficient and normalized cross-correlation between the transspine field and the free-field measurements. Simulation-corrected focusing methods reduced planar shift and improved Dice similarity and normalized cross-correlation but did not meet the threshold of statistical significance.

Transspine peak positive pressure values of ∼40% of free-field peak positive pressure were achieved, higher than the ∼30% transmission reported in Xu and O'Reilly (2018), and the ∼30% transmission anticipated by simulations in the 500 kHz spine-specific array design study (Xu and O'Reilly 2020). The improvement in pressure transmission may be due to the lower implemented frequency (400 kHz vs. 500–514 kHz).

For all beamforming methods, focal shift was largest in the *x* (anterior-posterior) direction. In the sagittal plane, the bulk of targeting improvements came from reductions in *z* direction (superior-inferior) shift. Gold standard hydrophone-corrected focusing, for example, reduced average *z* direction shift by 43% while reducing average *x* direction shift by only 6%. Ray acoustics beamforming, on the other hand, reduced *z* direction shift by 20% and failed to reduce *x* direction shift. Targeting improvements in the coronal plane were similarly dominated by reductions in *z* direction shift, although it should be noted that the initial *y* (left-right) shift in this plane was on average <0.25 mm even in the uncorrected geometric case. In a clinical setting, this anterior-posterior shift could deflect the focus away from the treatment target and towards the walls of the canal, resulting in undesirable heating in the bone.

It was observed that, on average, the 90% contour in the sagittal plane was shifted in the negative *x* direction, towards the vertebral body and away from the array (table 1). It is hypothesized that this shift is caused by the increase in bone thickness between the more lateral laminae and the more medial spinous process, with the posterior arch acting effectively as a lens. Since the spine-specific array is split into two panels, each positioned approximately 12 cm posterior to the target, the device can be thought of as two 64-element apertures that are focused unilaterally and whose beam profiles intersect in the canal. Given the distance between each aperture and the target, the beam is already largely focused by the time it intersects with vertebral bone (figure 7). On each side, the more medial portion of the focused beam will have a longer path through bone than the more lateral portion of the beam and will undergo a correspondingly larger phase shift, deflecting the beam laterally away from the centre of the canal. As a result, the intersection point of the two apertures is pushed towards the anterior wall of the canal, and the focus undergoes a corresponding anterior shift. Because each individual element illuminates a large portion of the vertebral arch, this deflection is difficult to compensate for.

Finally, it is notable that in some trials sagittal and coronal shift were well below 1 mm even using uncorrected geometric beamforming. Furthermore, while the accuracy of 90% contour is a prudent metric for ablative or thermal therapies, where it is essential that the point of maximum pressure intersect the target structure, for low-intensity applications it may be adequate for the 50% contour of the focus to intersect with the target. If care is taken to avoid overtreatment through the paralaminar spaces, some targets may not require phase correction for BSCB opening to be feasible.

4.2. Simulation phase error and the impact of unoccluded paths

Focusing performance was worst for targets adjacent to paralaminar acoustic windows. This effect was consistent across correction methods, suggesting that, in a therapeutic setting, new beamforming methods may be needed to mitigate unwanted off-target effects. In addition, several favourable sonication targets were identified for which coherent focusing was achievable even in the absence of aberration correction. These targets were located roughly at the vertical midpoint of the laminae in the lower thoracic segments (T7–T9 and T10–T12), away from both paralaminar spaces and overlapping layers of bone. In future work, it may be

advantageous to sonicate only through the most acoustically favourable path in a given vertebra, and target structures adjacent to that path using transosseous beam steering techniques (Clement and Hynynen 2002b). However, the limits of transosseous steering in the spinal canal have yet to be explored, and it is uncertain whether a sufficient steering range can be achieved to allow treatment of the entire spinal cord.

In three targets, simulation-corrected focusing substantially underperformed relative to the hydrophone-corrected gold standard. Two of these cases occurred in locations where the beam path was likely to intersect multiple layers of bone. In the remaining case, the beam appeared to intersect the steeply angled spinous process rather than the relatively flat laminae. As such, the poor performance of ray acoustics-corrected beamforming at these locations is consistent with the initial conditions of the model as described by Xu and O'Reilly, which considered a single large (5 cm), spherically focused transducer rather than many individual annular transducers. In the original model, vertebral mesh elements with normals that deviated by more than 60° away from the transducer axis were removed to isolate segments of the posterior and anterior surface of the lamina that were roughly plate-like in geometry (Xu and O'Reilly 2018). This assumption was valid because most of the sound propagating from a large, spherically-focused element passes through a small enough region of vertebra that the two-plate approximation holds. When considering smaller, unfocused annular elements at a relatively large distance from the target, however, the assumption may not hold. As such, model accuracy is greater when targeting through the broad, flat surfaces of the lower laminae, and worse when attempting to model propagation that intersects multiple bone layers or the steeply angled surfaces of the transverse and spinous processes.

The results of the forward pressure simulations provide further evidence of the impact of paravertebral acoustic windows on focal quality. Attempts at transspine focusing must consider the impact of unoccluded paths on targeting accuracy and focal intensity, which suggests that treatment planning for BSCB applications will always require some degree of preoperative field prediction. In future work, mitigation of unoccluded contributions could be achieved through the inclusion of anti-focus control points at the location of off-target lobes (Ebbini and Cain 1989, Seo and Lee 2009, Pulkkinen *et al* 2011). It should also be noted that if a therapeutic target is immediately adjacent to an acoustic window, it may be advantageous to focus directly through the window rather than the surrounding bone (Xu and O'Reilly 2020, Xu *et al* 2024). This potential reinforces the need for field prediction in the treatment planning process, to maximize treatment efficacy while sparing surrounding tissue.

Lastly, validation of the field predictions generated by the ray acoustics model show that it performs reasonably well at the 70% contour level in both sagittal and coronal planes. The drop in accuracy seen at the 90% contour level may stem from the sensitivity of the smaller contour to registration error, as well as the use of a steady-state model to predict the output of a pulsed sonication. The use of a short driving pulse may also have impacted the performance of ray acoustics-derived phase correction, as the model assumes a steady-state condition that is not necessarily achieved in a short pulse. As such, a more complex, time-domain model may produce improved phase corrections and higher-fidelity field simulations for an aperture driven with short pulses.

4.3. Clinical implications in spinal cord therapy

The outcome of this study has a number of clinical implications for spinal cord therapies. First, for some targets, bone-induced focal aberration is minimal. Although the potential for off-target contributions via paralaminar windows precludes attempts at uncorrected focusing for thermal or ablative applications, it may be possible to perform low-pressure, bubble mediated therapies such as BSCB opening without aberration correction. In such applications, it may be sufficient to use geometric focusing delays, and control exposures via passive acoustic mapping of bubble activity and the use of an acoustic emissions-based controller (O'Reilly and Hynynen 2012, Frizado and O'Reilly 2023). A limitation is that some targets may not be adequately treated with geometric focusing or the current correction method and strategies to address this subset should be investigated in future studies.

In stimulation or neuromodulation applications, where microbubbles are presumed to be absent, simulation-based methods may be needed to estimate in situ pressure. A recent *in silico* safety study of cervical neuromodulation found that small errors in the positioning of a posterior ultrasound array can greatly increase spine heating relative to target pressure, suggesting that accurate field predictions may be needed to prevent thermal damage (Xu *et al* 2024).

4.4. Limitations and sources of error

This study was subject to several limitations and sources of error. The first is registration error between the experimental setup and the simulation environment. Precautions were taken to minimize this error, including careful measurement and recreation of the dimensions of the experimental setup in SolidWorks and the integration of optical stages into the apparatus to allow for precise translations and rotations to be

applied to a column of vertebrae. However, the position of the array surface and the vertebral column in simulation space remained dependent on point-based registration using either a blunted needle or the tip of the needle hydrophone. Previous work with individual vertebrae used 9 landmarks per vertebra, for an estimated registration error of less than 1.3 mm relative to ground truth (Xu and O'Reilly 2018). Much of the vertebral anatomy is not accessible for registration when using the plates to clamp the column in place. Registration was achieved instead using four landmarks on the base of the anatomically superior plate in the column, and 8 points on the surface of the array housing. The smallest increment used for when positioning the hydrophone tip for registration was 0.1 mm, and experimental error for each landmark position can therefore be estimated as:

$$\mathrm{err} = \sqrt{0.1^2 + 0.1^2 + 0.1^2} = 0.17 \ \mathrm{mm}. \tag{8}$$

The standard deviation in landmark error can then be estimated as:

$$\mathrm{SD}_{\mathrm{err}} = \sqrt{\frac{\sum_{i=1}^{N} \mathrm{err}_i^2}{(N-1)}} \tag{9}$$

where N is the number of registration points. The estimated standard deviations in landmark position error are 0.12 mm for the superior plate in the column (4 registration points) and 0.05 mm for the array surface (8 registration points). Total positioning uncertainty can then be estimated as:

$$U = \sqrt{0.12^2 + 0.05^2} = 0.13 \ \mathrm{mm}. \tag{10}$$

The estimated positioning uncertainty is thus an order of magnitude smaller than the 2 mm vertical shifts applied to the column between trials. However, it should be noted that landmark positioning error can cause rotation of the column and/or array, leading to an amplified effect on the total registration. The true registration error is difficult to estimate given the limited number of landmarks recorded on the column. In future benchtop work involving stacked vertebrae, it may be necessary to devise a means of recording landmarks on each individual vertebra in the column.

An additional source of error was that, in all simulations, a uniform impulse response at 400 kHz was assumed for all elements. This is not always the case experimentally, as there may be variation in the maximum amplitude, frequency content, and length of ringdown observed in different elements in response to an identical input voltage. The frequency distribution of a pressure waveform measured at the free-field geometric focus was centred between 430 and 440 kHz (figure 4), an unaccounted-for frequency shift. Assuming an average laminar thickness of 5.4 mm and a bulk laminar speed of sound of 1670 m s^{-1}, (Xu and O'Reilly 2022) the frequency shift is estimated to have introduced a 1% error in phase shift predictions. Furthermore, although an additional layer of bone was included in the simulation along propagation paths that intersected multiple vertebrae, the ray acoustics model used here has only been validated in single vertebra experiments. Additional refinement of the model, or a shift to a full-wave, time-domain simulation method, may be needed in order to accurately represent the propagation of the implemented short pulses across multiple layers of bone.

Finally, there is the issue of hydrophone directivity. The vertical orientation of the spinal canal requires the hydrophone to remain aligned with the *z*-axis of the experimental setup. It is likely that, in both waveform measurements and field scans, the hydrophone response includes some bias toward waves arriving from smaller incident angles. In future work, the extent to which hydrophone directivity impacts free-field measurements and amplitude normalization apodizations could be estimated by recording measurements at a range of incident angles. However, in these experiments directivity was accounted for in the methods used to calculate focal shift and changes in intensity. All experimentally recorded changes in focal location and intensity were measured relative to a free-field measurement obtained with a hydrophone oriented in the same manner as in the spine experiments. Hydrophone directivity may still have affected the transspine measurement if the spine substantially changed the propagation direction of the incident waves, but this cannot be measured with the current experimental setup. The impact of directivity on transvertebral measurements could be estimated if the hydrophone were oriented perpendicular to the interior wall of the vertebral canal, but this is not possible with intact vertebrae.

5. Conclusion

This study evaluated the performance of simulation-corrected beamforming with a multilayered, steady-state ray acoustics model for *ex vivo* transspine focusing. The ray acoustics model was evaluated against a geometrically-focused baseline and hydrophone-corrected gold standard. Although improvement was seen in sagittal and coronal focal shift when simulation-based corrections were applied, the simulation-based method did not achieve statistically significant improvements in focal shift or target pressure over the geometric focusing baseline when focusing bilaterally through a column of *ex vivo* vertebrae. *Post hoc* analysis found that transspine focusing feasibility varied with target location, with favourable targets requiring little to no phase correction for coherent focusing and unfavorable targets showing poor performance even when gold standard phase correction was applied. The performance of ray acoustics-derived phase correction was similarly target-dependent, as model performance decreased for propagation paths inferior or superior to the vertical midpoint of the vertebral laminae. Notably, some targets saw focal shifts below 1 mm even in the uncorrected case, suggesting that low-intensity applications such as BSCB opening may be possible even in the absence of CT-derived phase correction. Future *in vivo* work should investigate both uncorrected and simulation-corrected BSCB opening in large animal models, while future *in silico* work should examine the possibility of improving simulation-corrected transspine focusing with transosseous beam steering and anti-focus control points.

Data availability statement

The data cannot be made publicly available upon publication because they are not available in a format that is sufficiently accessible or reusable by other researchers. The data that support the findings of this study are available upon reasonable request from the authors.

Acknowledgment

Ethical statement

This project makes use of anonymous human materials from deceased individuals and therefore does not meet the NIH definition of 'Human Subject Research'. Experiments with *ex vivo* human vertebrae were performed with prior approval from the Sunnybrook Health Sciences Centre Research Ethics Board, Project Identification Number 2693.

ORCID iDs

David Martin ⬤ https://orcid.org/0009-0002-7436-3157
Rui Xu ⬤ https://orcid.org/0000-0003-1606-0932
Max Dressler ⬤ https://orcid.org/0009-0006-6905-6055

References

Ando T, Sato S, Toyooka T, Uozumi Y, Nawashiro H, Ashida H and Obara M 2011 Site-specific gene transfer into the rat spinal cord by photomechanical waves *J. Biomed. Opt.* **16** 108002

Aubry J F, Pernot M, Marquet F, Tanter M and Fink M 2008 Transcostal high-intensity-focused ultrasound: ex vivo adaptive focusing feasibility study *Phys. Med. Biol.* **53** 2937–51

Aubry J-F, Tanter M, Pernot M, Thomas J-L and Fink M 2003 Experimental demonstration of noninvasive transskull adaptive focusing based on prior computed tomography scans *J. Acoust. Soc. Am.* **113** 84–93

Beccaria K, Sabbagh A, de Groot J, Canney M, Carpentier A and Heimberger A B 2021 Blood–brain barrier opening with low intensity pulsed ultrasound for immune modulation and immune therapeutic delivery to CNS tumors *J. Neurooncol.* **151** 65–73

Bhimreddy M *et al* 2023 Disruption of the blood-spinal cord barrier using low-intensity focused ultrasound in a rat model *J. Vis. Exp.* **193** 65113

Busscher I, Ploegmakers J J W, Verkerke G J and Veldhuizen A G 2010 Comparative anatomical dimensions of the complete human and porcine spine *Eur. Spine J.* **19** 1104–14

Carpentier A *et al* 2016 Y and Idbaih A 2016 Clinical trial of blood-brain barrier disruption by pulsed ultrasound *Sci. Transl. Med.* **8** 343re2

Chen K-T, Lin Y-J, Chai W-Y, Lin C-J, Chen P-Y, Huang C-Y, Kuo J S, Liu H-L and Wei K-C 2020 Neuronavigation-guided focused ultrasound (NaviFUS) for transcranial blood-brain barrier opening in recurrent glioblastoma patients: clinical trial protocol *Ann. Transl. Med.* **8**

Clement G T and Hynynen K 2002a A non-invasive method for focusing ultrasound through the human skull *Phys. Med. Biol.* **47** 1219–36

Clement G T and Hynynen K 2002b Micro-receiver guided transcranial beam steering *IEEE Trans. Ultrason. Ferroelectr. Freq. Control* **49** 447–53

Cross C G, Payne A H, Hawryluk G W, Haag-Roeger R, Cheeniyil R, Brady D, Odéen H, Minoshima S, Cross D J and Anzai Y 2021 Technical Note: Quantification of blood-spinal cord barrier permeability after application of magnetic resonance-guided focused ultrasound in spinal cord injury *Med. Phys.* **48** 4395–401

Dice L R 1945 Measures of the amount of ecologic association between species *Ecology* **26** 297–302

Ebbini E S and Cain C A 1989 Multiple-focus ultrasound phased-array pattern synthesis: optimal driving-signal distributions for hyperthermia *IEEE Trans. Ultrason. Ferroelectr. Freq. Control* **36** 540–8

Fletcher S M P, Choi M, Ogrodnik N and O'Reilly M A 2020 A porcine model of transvertebral ultrasound and microbubble-mediated blood-spinal cord barrier opening *Theranostics* **10** 7758–74

Fletcher S M P and O'Reilly M A 2018 Analysis of multifrequency and phase keying strategies for focusing ultrasound to the human vertebral canal *IEEE Trans. Ultrason. Ferroelectr. Freq. Control* **65** 2322–31

Fletcher S M P, Ogrodnik N and O'Reilly M A 2019 Enhanced detection of bubble emissions through the intact spine for monitoring ultrasound-mediated blood-spinal cord barrier opening *IEEE Trans. Biomed. Eng.* **67** 1387–96

Frizado A Paul and O'Reilly M Anne 2023 A numerical investigation of passive acoustic mapping for monitoring bubble-mediated focused ultrasound treatment of the spinal cord *J. Acoust. Soc. Am.* **153** 2271–84

Fry F J 1977 Transkull transmission of an intense focused ultrasonic beam *Ultrasound Med. Biol.* **3** 179–84

Fry F J and Barger J E 1978 Acoustical properties of the human skull *J. Acoust. Soc. Am.* **63** 1576–90

Hasgall P A, Di Gennaro F, Baumgartner C, Neufeld E, Lloyd B, Gosselin M C, Payne D, Klingenböck A and Kuster N 2022 IT'IS Database for thermal and electromagnetic parameters of biological tissues (https://doi.org/10.13099/VIP21000-04-1)

Horn B K P, Hilden H M and Negahdaripour S 1988 Closed-form solution of absolute orientation using orthonormal matrices *J. Opt. Soc. Am.* A **5** 1127

Huang Y *et al* 2022 Cavitation feedback control of focused ultrasound blood-brain barrier opening for drug delivery in patients with Parkinson's disease *Pharmaceutics* **14** 2607

Hynynen K, McDannold N, Vykhodtseva N and Jolesz F A 2001 Noninvasive MR imaging-guided focal opening of the blood-brain barrier in rabbits *Radiology* **220** 640–6

Jiménez-Gambín S, Jiménez N, Benlloch J M and Camarena F 2019 Holograms to focus arbitrary ultrasonic fields through the skull *Phys. Rev. Appl.* **12** 014016

Kim E, Kum J and Kim H 2022 Trans-spinal focused ultrasound stimulation selectively modulates descending motor pathway *IEEE Trans. Neural Syst. Rehabil. Eng.* **30** 314–20

Leung S A, Moore D, Gilbo Y, Snell J, Webb T D, Meyer C H, Miller G W, Ghanouni P and Butts Pauly K 2022 Comparison between MR and CT imaging used to correct for skull-induced phase aberrations during transcranial focused ultrasound *Sci. Rep.* **12** 13407

Leung S A, Moore D, Webb T D, Snell J, Ghanouni P and Butts Pauly K 2021 Transcranial focused ultrasound phase correction using the hybrid angular spectrum method *Sci. Rep.* **11** 6532

Lewis J P (Industrial L & M) 1995 Fast normalized cross-correlation template matching by cross *Vision Interface* **1995**

Liao Y H, Chen M X, Chen S C, Luo K X, Wang B, Ao L J and Liu Y 2022 Low-intensity focused ultrasound alleviates spasticity and increases expression of the neuronal K-Cl cotransporter in the L4–L5 sections of rats following spinal cord injury *Front. Cell Neurosci.* **16** 882127

Liao Y H, Chen M X, Chen S C, Luo K X, Wang B, Liu Y, Ao L J and Zhang F 2021a Effects of noninvasive low-intensity focus ultrasound neuromodulation on spinal cord neurocircuits in vivo *Evid. Based Complement. Alternat. Med.* **2021** 1–16

Liao Y H, Wang B, Chen M X, Liu Y, Ao L J and Wang X-Q 2021b LIFU alleviates neuropathic pain by improving the KCC2Expression and inhibiting the CaMKIV-KCC2Pathway in the L4-L5 section of the spinal cord *Neural Plast.* **2021** 1–10

Limthongkul W, Karaikovic E E, Savage J W and Markovic A 2010 Volumetric analysis of thoracic and lumbar vertebral bodies *Spine J.* **10** 153–8

Lipsman N *et al* 2018 Blood–brain barrier opening in Alzheimer's disease using MR-guided focused ultrasound *Nat. Commun.* **9** 1–8

Maimbourg G, Houdouin A, Deffieux T, Tanter M and Aubry J F 2018 3D-printed adaptive acoustic lens as a disruptive technology for transcranial ultrasound therapy using single-element transducers *Phys. Med. Biol.* **63** 025026

Maimbourg G, Houdouin A, Deffieux T, Tanter M and Aubry J F 2020 Steering capabilities of an acoustic lens for transcranial therapy: numerical and experimental studies *IEEE Trans. Biomed. Eng.* **67** 27–37

Manuel T J *et al* 2024 Ultra-short time-echo based ray tracing for transcranial focused ultrasound aberration correction in human calvaria *Phys. Med. Biol.* Epub ahead of print

Meng Y *et al* 2021 MR-guided focused ultrasound enhances delivery of trastuzumab to Her2-positive brain metastases *Sci. Transl. Med.* **13** eabj4011

Montero A S *et al* 2019 Ultrasound-induced blood–spinal cord barrier opening in rabbits *Ultrasound Med. Biol.* **45** 2417–26

Montero A-S *et al* 2024 Effect of ultrasound-mediated blood-spinal cord barrier opening on survival and motor function in females in an amyotrophic lateral sclerosis mouse model *EBioMedicine* **106** 105235

O'Reilly M A, Chinnery T, Yee M L, Wu S K, Hynynen K, Kerbel R S, Czarnota G J, Pritchard K I and Sahgal A 2018 Preliminary investigation of focused ultrasound-facilitated drug delivery for the treatment of leptomeningeal metastases *Sci. Rep.* **8** 1–8

O'Reilly M A and Hynynen K 2012 Blood-brain barrier: Real-time feedback-controlled focused ultrasound disruption by using an acoustic emissions–based controller *J. Radiol.* **263** 96–106

Oakden W, Kwiecien J M, O'Reilly M A, Dabrowski W, Whyne C, Finkelstein J, Hynynen K and Stanisz G J 2015 Quantitative MRI in a non-surgical model of cervical spinal cord injury *NMR Biomed.* **28** 925–36

Payne A H, Hawryluk G W, Anzai Y, Odéen H, Ostlie M A, Reichert E C, Stump A J, Minoshima S and Cross D J 2017 Magnetic resonance imaging-guided focused ultrasound to increase localized blood-spinal cord barrier permeability *Neural. Regen. Res.* **12** 2045–9

Pichardo S, Moreno-Hernández C, Andrew Drainville R, Sin V, Curiel L and Hynynen K 2017 A viscoelastic model for the prediction of transcranial ultrasound propagation: application for the estimation of shear acoustic properties in the human skull *Phys. Med. Biol.* **62** 6938–62

Pichardo S, Sin V W and Hynynen K 2011 Multi-frequency characterization of the speed of sound and attenuation coefficient for longitudinal transmission of freshly excised human skulls *Phys. Med. Biol.* **56** 219–50

Pulkkinen A, Huang Y, Song J and Hynynen K 2011 Simulations and measurements of transcranial low-frequency ultrasound therapy: skull-base heating and effective area of treatment *Phys. Med. Biol.* **56** 4661–83

Rezai A R *et al* 2024 Ultrasound blood–brain barrier opening and aducanumab in Alzheimer's disease *N. Engl. J. Med.* **390** 55–62

Seo J and Lee J 2009 Anti-foci for focused ultrasound *Int. J. Hyperthermia* **25** 566–80

Shahar R, Zaslansky P, Barak M, Friesem A A, Currey J D and Weiner S 2007 Anisotropic Poisson's ratio and compression modulus of cortical bone determined by speckle interferometry *J. Biomech.* **40** 252–64

Shimamura M, Sato N, Taniyama Y, Kurinami H, Tanaka H, Takami T, Ogihara T, Tohyama M, Kaneda Y and Morishita R 2005 Gene transfer into adult rat spinal cord using naked plasmid DNA and ultrasound microbubbles *J. Gene Med.* **7** 1468–74

Song W, Jayaprakash N, Saleknezhad N, Puleo C, Al-Abed Y, Martin J H and Zanos S 2024 Transspinal focused ultrasound suppresses spinal reflexes in healthy rats *Neuromodulation* **27** 614–24

Song Z, Wang Z, Shen J, Xu S and Hu Z 2017 Nerve growth factor delivery by ultrasound-mediated nanobubble destruction as a treatment for acute spinal cord injury in rats *Int. J. Nanomed.* **12** 1717–29

Sørensen T 1948 A method of establishing groups of equal amplitude in plant sociology based on similarity of species content and its application to analyses of the vegetation on danish commons *Kongelige Danske Videnskabernes Selskab* **5** 1–34

Tsehay Y *et al* 2023 Low-intensity pulsed ultrasound neuromodulation of a rodent's spinal cord suppresses motor evoked potentials *IEEE Trans. Biomed. Eng.* **70** 1992–2001

Wachsmuth J, Chopr R and Hynynen K 2009 Feasibility of transient image-guided blood-spinal cord barrier disruption *AIP Conf. Proc.* **1113** 256–9

Wang B, Zhao H, Chen M, Chen S, Liao Y, Tang X, Ao L and Liu Y 2023 Proteomics reveals the effect of low-intensity focused ultrasound on spasticity after spinal cord injury *Turk. Neurosurg.* **33** 77–86

Weber-Adrian D *et al* 2015 Gene delivery to the spinal cord using MRI-guided focused ultrasound *Gene Ther.* **22** 568–77

White P J, Palchaudhuri S, Hynynen K and Clement G T 2007 The effects of desiccation on skull bone sound speed in porcine models *IEEE Trans. Ultrason. Ferroelectr. Freq. Control* **54** 1708–10

Xu R, Bestmann S, Treeby B E and Martin E 2024 Strategies and safety simulations for ultrasonic cervical spinal cord neuromodulation *Phys. Med. Biol.* **69** 125011

Xu R, Martin D and O'Reilly M A 2021 Array-based beamforming to the vertebral canal: demonstration of feasibility *IEEE Int. Ultrasonics Symp., IUS*

Xu R and O'Reilly M A 2018 Simulating transvertebral ultrasound propagation with a multi-layered ray acoustics model *Phys. Med. Biol.* **63** 145017

Xu R and O'Reilly M A 2020 A spine-specific phased array for transvertebral ultrasound therapy: design and simulation *IEEE Trans. Biomed. Eng.* **67** 256–67

Xu R and O'Reilly M A 2022 Establishing density-dependent longitudinal sound speed in the vertebral lamina *J. Acoust. Soc. Am.* **151** 1516–31

Yushkevich P A, Gao Y and Gerig G 2016 ITK-SNAP: an interactive tool for semi-automatic segmentation of multi-modality biomedical images *Proc. Annual Int. Conf. of the IEEE Engineering in Medicine and Biology Society, EMBS* vol 2016